


Addressing preferred specimen orientation in single-particle cryo-EM through tilting

Yong Zi Tan^{1,2}, Philip R Baldwin¹, Joseph H Davis³, James R Williamson³, Clinton S Potter^{1,2}, Bridget Carragher^{1,2} & Dmitry Lyumkis⁴

We present a strategy for tackling preferred specimen orientation in single-particle cryogenic electron microscopy by employing tilts during data collection. We also describe a tool to quantify the resulting directional resolution using 3D Fourier shell correlation volumes. We applied these methods to determine the structures at near-atomic resolution of the influenza hemagglutinin trimer, which adopts a highly preferred specimen orientation, and of ribosomal biogenesis intermediates, which adopt moderately preferred orientations.

Recent methodological advances in single-particle cryogenic electron microscopy (cryo-EM) have enabled the elucidation of biological macromolecular structures to near-atomic resolutions. Despite numerous advances, preferred particle orientation represents a recurring problem for the cryo-EM field^{1,2}. Ideally, macromolecules adopt random orientations within a layer of vitreous ice supported by an EM grid; which, in principle, results in isotropic distribution of angular projection orientations. This, however, is rarely true in practice, presumably on account of surface properties of the molecules that cause specific regions to preferentially adhere to the air–water interface or substrate support³. Preferred specimen orientations result in nonuniform distribution of angular projection views of the individual particles, a proportional undersampling of Fourier components within the final reconstruction, and an overall loss of resolution parallel to the preferred orientation axis (a ‘smearing effect’ of the map⁴). In extreme cases, reconstructions have large amounts of missing information in Fourier space, or they may completely misrepresent the true structure of the imaged object. These effects can be collectively described by directional resolution anisotropy⁵.

Prior efforts have attempted to address preferred specimen orientation in cryo-EM using a number of different approaches (Supplementary Note 1). Here, we present a sample-independent

and generally applicable strategy to address this problem by collecting data at defined tilts (Supplementary Note 2 and Supplementary Fig. 1). Whereas tilt-based approaches have previously been employed in single-particle studies, resulting reconstructions have generally been limited to low-to-moderate resolution^{6–10}. Our implementation shows that it is now possible to obtain near-atomic resolution structures of preferentially oriented single-particle samples. We also introduce a tool to quantitatively assess directional resolution anisotropy of density maps using an algorithm based on the conventional Fourier shell correlation (FSC) analysis (see Online Methods). This program generates a set of 1D FSC curves computed over distinct angular directions and combines them into a 3D array that we term the 3D FSC. We evaluate this program using synthetic data and show that an isotropic projection distribution produces a spherical 3D FSC (Supplementary Note 3 and Supplementary Fig. 2).

Several aspects of our strategy deserve mention. First, individual fields of view are exposed only once; in other words, all aspects of data collection are performed as in conventional single-particle analysis, with the sole exception that the goniometer is set to a defined nominal tilt angle. Second, contrast transfer function (CTF) estimation must take into account the defocus gradient across individual micrographs to obtain per-particle CTF values. We estimate per-particle CTFs using GCTF¹¹ for the described results, which provided the highest resolution reconstructions among the strategies evaluated (see Online Methods). Third, we used gold substrates to minimize beam-induced movement at tilt¹² and motion correction of individual movie frames to account for any residual movements¹³. Fourth, to account for increased ice thickness and particle contrast reduction at tilt, we used a high-dose imaging strategy and exposure filtered the resulting frames¹⁴. Finally, the tilt collection scheme is independent of the sample or buffer and can be universally used.

We tested our tilt collection strategy on the soluble portion of the small, 150-kDa influenza hemagglutinin (HA) trimer, which exhibits a single, highly preferred ‘top’ orientation on vitrified cryo-EM grids (Supplementary Note 4 and Supplementary Fig. 3). To evaluate how expected improvements in resolution and density isotropy would counterbalance the practical drawbacks associated with tilting, we collected images at 0°, 10°, 20°, 30°, 40°, and 50° tilts; equally divided the data sets; refined each set in an identical manner; and compared the resulting maps (Supplementary Fig. 4). 3D FSCs and their corresponding sphericities were calculated for each reconstruction to evaluate directional isotropy. Distinct directional resolution values obtained at a nominal cutoff threshold (0.143 (ref. 15)) were plotted as a histogram onto a

¹The National Resource for Automated Molecular Microscopy, Simons Electron Microscopy Center, New York Structural Biology Center, New York, New York, USA.

²Department of Biochemistry and Molecular Biophysics, Columbia University, New York, New York, USA. ³Department of Integrative Structural and Computational Biology, Department of Chemistry, and The Skaggs Institute for Chemical Biology, The Scripps Research Institute, La Jolla, California, USA. ⁴Laboratory of Genetics and Helmsley Center for Genomic Medicine, The Salk Institute for Biological Studies, La Jolla, California, USA. Correspondence should be addressed to D.L. (dlyumkis@salk.edu).

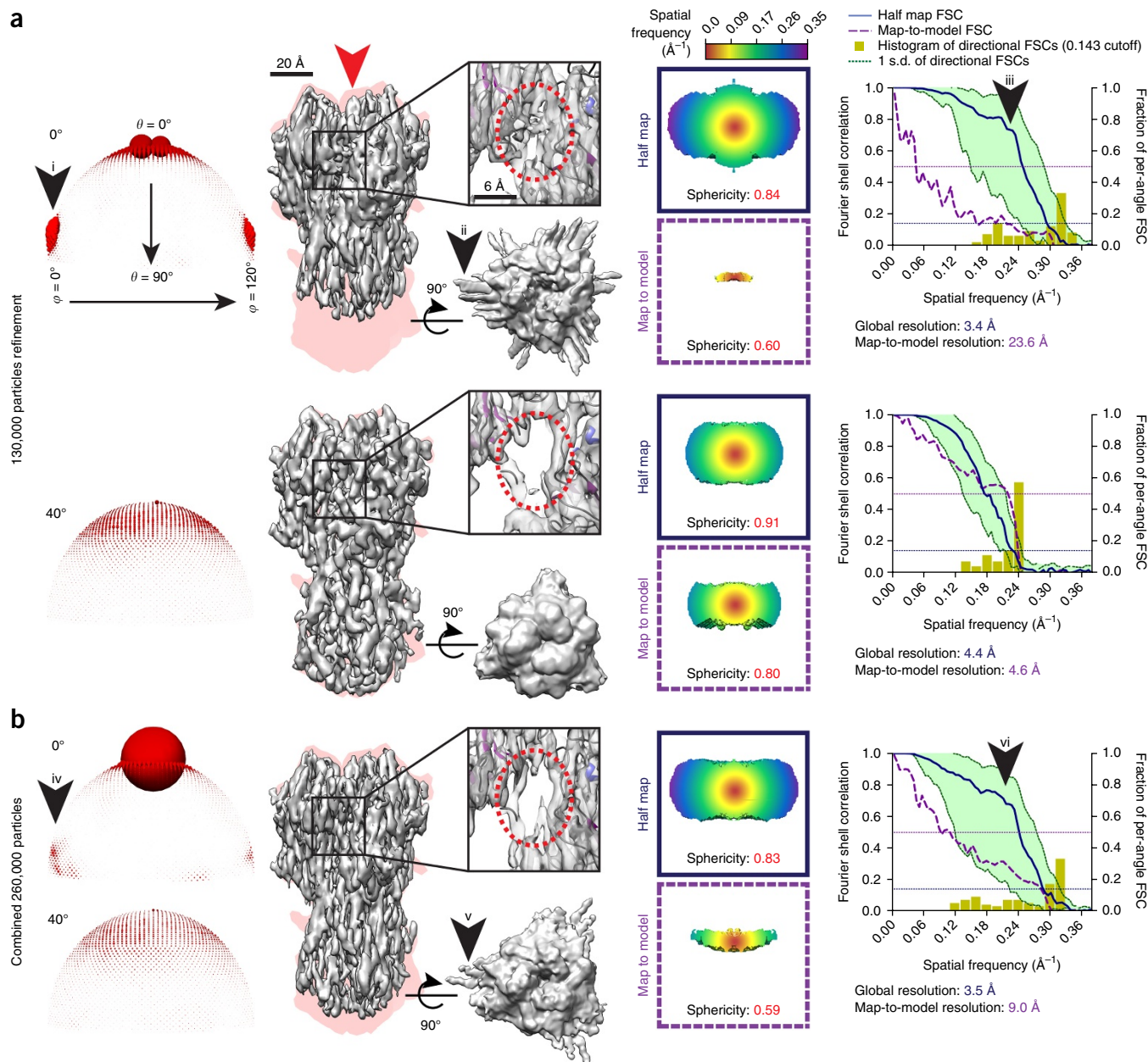


Figure 1 | Preferred orientation results in artifacts that can be overcome by tilting. **(a,b)** Shown from left to right: Euler angle distribution; side view of the reconstruction (in gray, the direction of preferred orientation is indicated by the red arrowhead) superimposed onto a projection of the envelope of the HA trimer crystal structure (in pink), displayed alongside a top view thresholded at a lower value and a closeup of a particular region; half-map and map-to-model 3D FSCs; plots of the global half-map FSC (solid blue line) and map-to-model FSC (dotted purple line) together with the spread of directional resolution values defined by $\pm 1\sigma$ from the mean (green area encompassed by dotted green lines, left axis) and a histogram of 100 such values evenly sampled over the 3D FSC (yellow bars, right axis). Arrows i and iv indicate presence of false side views, arrowhead ii and v indicate streaking in the unsharpened maps, and arrows iii and vi indicate bumps in the global FSC, all of which result from overfitting. **(a)** Comparison of HA trimer reconstructions refined independently from untilted images (130,000 particles) or from 40°-tilted images (130,000 particles). **(b)** HA trimer reconstruction refined from 260,000 particles combined from both data sets.

conventional FSC plot and compared with the global resolution. Map-to-model 3D directional and global FSCs were also included to specifically evaluate external consistency to a common reference (X-ray structure of HA, PDB: 3WHE), and the FSC external consistency contrasts with the internal self-consistency of conventional half-map-based resolutions. We observe that, in the absence of any tilt or at lower angle tilts, reconstructions exhibit a bulk loss of axial density concomitant with elongation along the Z-axis

characteristic of poor Z-axis resolution. As expected, at higher angle tilts, these effects are ameliorated with improved isotropy and are quantitatively captured by both half-map and especially map-to-model 3D FSCs, which in these examples provide a better evaluation of the accuracy of the reconstruction (**Supplementary Fig. 4**). Although nominal resolution gains were only observed up to 20° tilts using half-map FSCs, map-to-model FSCs continued to show significant improvements to the medium resolution

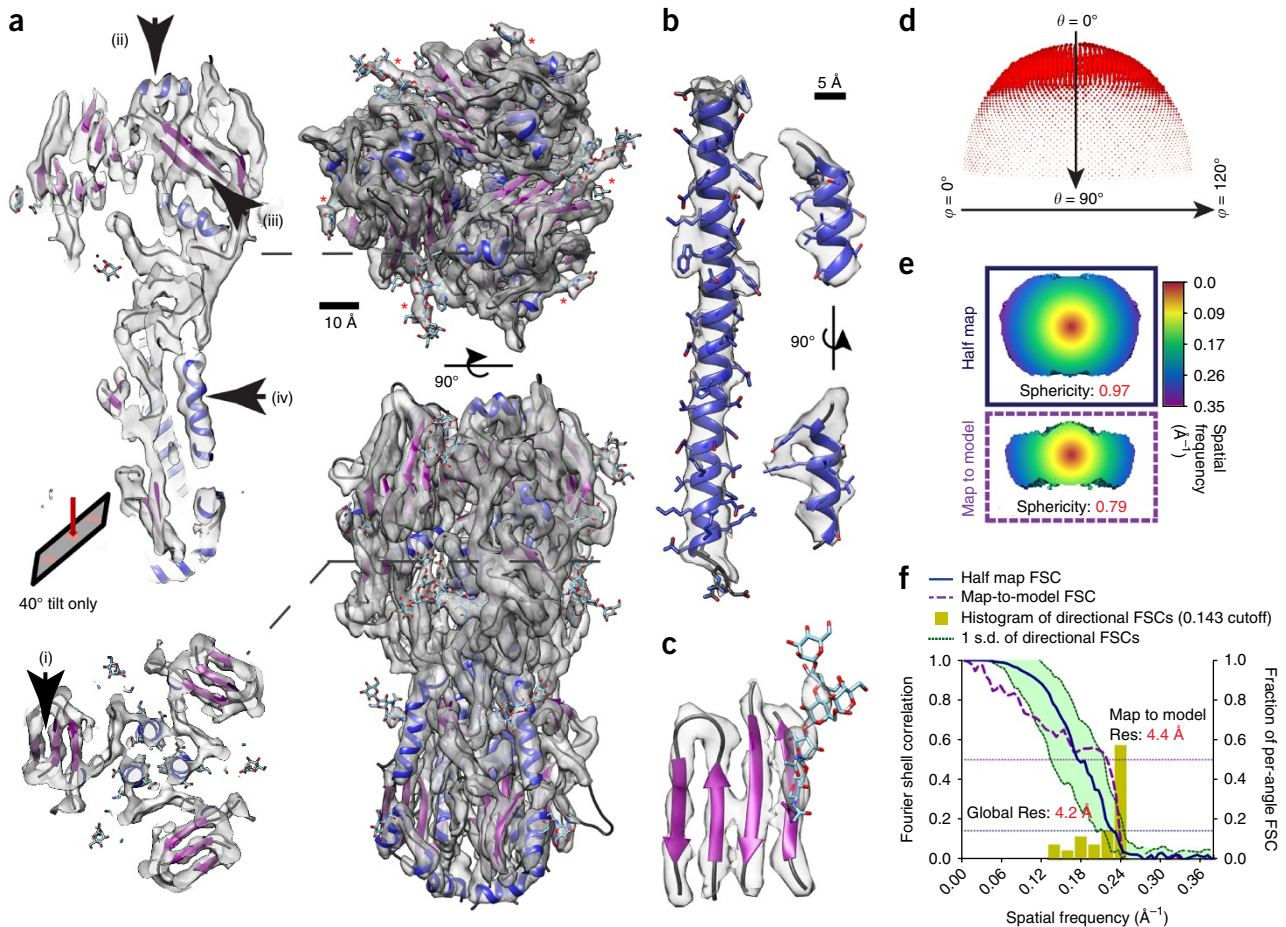


Figure 2 | Tilting enables recovery of near-atomic-resolution information from a data set of the highly preferentially oriented HA trimer. **(a)** Top view, side view, and respective slices through the 3D reconstruction of the HA trimer from 40°-tilted data. Representative glycan densities (red asterisks) are indicated. The separation of the **(a, i)** beta strands and **(a, ii)** alpha-helical pitch are well resolved if perpendicular to the direction of preferred orientation; **(a, iii)** and **(a, iv)** otherwise, they are slightly less defined. **(b)** Map density of two alpha helices (residues 402–458 and residues 105–115) and **(c)** a beta sheet (residues 162–170, 200–215, 240–249). **(d)** Euler angle distribution of the reconstruction. **(e)** Slice through 3D FSC of the reconstruction thresholded at 0.143 cutoff, as well as the map-to-model 3D FSC thresholded at 0.5 cutoff. Sphericity of the 3D FSC is indicated. **(f)** Graphs showing the spread of 3D FSC values overlaid on global half-map and map-to-model curves.

features at both 30° and 40° tilts, at the expense of high-resolution information. These results are consistent with the general idea that the overall fidelity of the maps characterized by low-resolution features improves with better density isotropy, but that high-resolution features suffer from the practical disadvantages associated with tilting.

Having observed quantitative improvements in global and directional resolution from HA data collected at high tilt angles, we proceeded to evaluate the possibility of using tilts for near-atomic-resolution single-particle analysis. A larger stack of particles from untilted (control) and 40°-tilted micrographs were collected and processed using the gold-standard refinement approach implemented within the latest generation software¹⁶ to produce maps (**Fig. 1a**) at nominally near-atomic resolution (3.4 Å and 4.4 Å, respectively). Visually, however, the reconstruction from untilted images was severely elongated along the Z-axis, and this produced artifactual densities and influenced apparent missing axial density at typical display thresholds. In contrast, the reconstruction from 40°-tilted images was a far more accurate representation of the real HA trimer structure. Furthermore, the reconstruction from untilted images displayed signs of overfitting. These signs,

largely absent in the reconstruction from tilted images, included (i) streaking at low-density thresholds (**Fig. 1** arrows ii, v); (ii) a sharp drop (**Fig. 1** arrows iii, vi) that is characteristic of overfitting exhibited by the global FSC¹⁷; and, most tellingly, (iii) the map-to-model global and 3D FSCs were much worse than the half-map FSCs. We reasoned that this overfitting also likely caused the side views within the Euler distribution plot (**Supplementary Fig. 5**). To test this, we combined the particles from untilted and tilted images to maintain a more accurate density throughout refinement (**Fig. 1b**). The same particles from untilted images that appeared as side views were now mostly classified as top views (compare arrows i and iv in **Fig. 1a,b**), which supported the conclusion that the highly anisotropic data set also led to some overfitting. Furthermore, the combined reconstruction showed that, despite doubling the number of particles, the resulting density and its associated resolutions (measured using an external reference) actually worsened (i.e., more elongation and signs of overfitting). These results demonstrate that preferred orientation can result in a reconstruction with apparent high resolution that is completely incorrect. At 40° tilts, and for this particular data set, the problem is largely resolved, and only a

small discrepancy in nominal resolution (~ 0.2 Å) exists between the map-to-model and half-map FSCs. The issue of directional resolution anisotropy is also alleviated.

Using the entire particle stack from 40°-tilted images, we obtained a reconstruction resolved to 4.2 and 4.4 Å using half-map and map-to-model criteria, respectively (Fig. 2). All image-processing operations, including the generation of an initial model, were performed *de novo*. The resulting map exhibited regions with bulky side chains, glycans, alpha-helical pitch, and beta-strand separation (Fig. 2). The missing cone, although still present, did not significantly affect the interpretability of the reconstruction, a scenario that is qualitatively similar to our synthetic data results comparing 60° and 90° tilts (Supplementary Fig. 2).

To test the generality of our approach, we applied our tilted collection strategy to bacterial large ribosomal subunit assembly intermediates¹⁸ that also exhibit preferred orientation, although less severely than HA (Supplementary Figs. 6–10). While the exact gains differed slightly across the four structural intermediates (superclasses), in part on account of different degrees of preferred orientation, we consistently observed an improvement in global and directional resolution with tilts, nominally ranging from ~ 0.2 – 0.7 Å, as well as expected improvements to isotropy (Supplementary Fig. 11). To determine the limits of tilting, we refined a data set from 50°-tilted images combined from homogeneous regions within all four superclasses, and we focused on mutually occupied ribosomal proteins. Using 17,170 particles, we resolved multiple proteins to ~ 4 – 5 Å resolution, with the best regions at ~ 4.2 Å; and the reconstruction was characterized by a nearly spherical 3D FSC (Supplementary Fig. 12).

The optimal collection strategy is a trade-off between degree of directional isotropy (higher tilts lead to better Fourier space sampling) and resolution (higher tilts lead to loss of high-spatial-frequency information). Based on our experiments, samples adopting extreme preferred orientations benefit from data collection at a single high tilt because of the amount of missing Fourier information. Incorporation of untilted data, without proper weighting, may lead to overfitting. It will thus be useful to incorporate anisotropic filters and orientation-weighting schemes during density refinement¹⁹ or reconstruction²⁰. For samples adopting less preferred orientations, smaller tilt angles, or combinations of tilt angles, this method provides improvements in both isotropy and global resolution. We thus conclude that single-particle data characterized by preferred orientation may generally be collected using some tilts, especially as the practical issues associated with tilting are addressed in future work.

As is widely accepted, global resolution alone is insufficient to determine map quality. Figure 1 and Supplementary Figure 11d,e demonstrate that smearing along the preferred orientation axis—a manifestation of directional anisotropy—obscures features like beta-strand separation and alpha-helical pitch. Importantly, loss of directional resolution may adversely affect researchers' ability to build and/or refine models into EM density maps. In addition to displaying Euler angle distributions, quantitative directional isotropy analysis should thus be a useful metric for evaluating cryo-EM density maps (Supplementary Fig. 13).

In conclusion, we demonstrate that tilted cryo-EM single-particle analysis quantitatively improves directional isotropy in samples exhibiting preferred orientation. We also present the 3D FSC program, which provides a method to evaluate the degree of

resolution anisotropy in any single-particle cryo-EM reconstruction. These methods, as they are sample independent and simple to implement, should be immediately applicable to many preferentially oriented cryo-EM specimens, including integral membrane proteins²¹.

METHODS

Methods, including statements of data availability and any associated accession codes and references, are available in the [online version of the paper](#).

Note: Any Supplementary Information and Source Data files are available in the online version of the paper.

ACKNOWLEDGMENTS

We thank N. Grigorieff, T. Grant, A. Rohou, A. Cheng and A. Noble for their invaluable advice; T. Goddard for incorporating the result of 3D FSC into UCSF Chimera. Molecular graphics and analyses were performed with the UCSF Chimera package (supported by NIGMS P41-GM103311). We thank B. Anderson and J.C. Ducom at TSRI for help with EM data collection and network infrastructure; and we thank F. Dwyer for computational support at the Salk Institute. The work was supported by Agency for Science, Technology and Research Singapore (to Y.Z.T.); the Leona M. and Harry B. Helmsley Charitable Trust Grant 2017-PG-MED001 (to D.L.); the US National Institutes of Health (NIH) (DP5 OD021396-01 to D.L.); the Jane Coffin Child's Foundation postdoctoral fellowship (to J.H.D.); the National Institute of Aging K99 transitional award (AG050749 to J.H.D.); National Institute of General Medical Sciences (GM103310 to C.S.P. and B.C.; GM053757 to J.R.W.); and Simons Foundation (349247 to C.S.P. and B.C.).

AUTHOR CONTRIBUTIONS

D.L. conceived the idea for this study. B.C. and C.P. provided guidance throughout the study. Y.Z.T. and D.L. performed the cryo-EM experiments, data collection, processing and analysis. D.L. and Y.Z.T. generated the synthetic data sets. P.R.B. and Y.Z.T. coded the 3D FSC program suite. J.H.D. and J.R.W. provided the L17-depleted 50S ribosomal samples. Y.Z.T. and D.L. wrote the manuscript with input from all authors.

COMPETING FINANCIAL INTERESTS

The authors declare no competing financial interests.

Reprints and permissions information is available online at <http://www.nature.com/reprints/index.html>. Publisher's note: Springer Nature remains neutral with regard to jurisdictional claims in published maps and institutional affiliations.

- Glaeser, R.M. *Nat. Methods* **13**, 28–32 (2016).
- Glaeser, R.M. & Han, B.-G. *Biophys. Rep.* <http://dx.doi.org/10.1007/s41048-016-0026-3> (2016).
- Taylor, K.A. & Glaeser, R.M. *J. Struct. Biol.* **163**, 214–223 (2008).
- Barth, M., Bryan, R.K. & Hegerl, R. *Ultramicroscopy* **31**, 365–378 (1989).
- Penczek, P.A. & Frank, J. in *Electron Tomography* (ed. Frank, J.) 307–330 (Springer, 2007).
- Yip, C.K., Murata, K., Walz, T., Sabatini, D.M. & Kang, S.A. *Mol. Cell* **38**, 768–774 (2010).
- Bartesaghi, A., Lecumberry, F., Sapiro, G. & Subramaniam, S. *Structure* **20**, 2003–2013 (2012).
- Radermacher, M., Wagenknecht, T., Verschoor, A. & Frank, J. *J. Microsc.* **146**, 113–136 (1987).
- Leschziner, A.E. & Nogales, E. *J. Struct. Biol.* **153**, 284–299 (2006).
- Su, M. *et al. Sci. Adv.* **3**, e1700325 (2017).
- Zhang, K. *J. Struct. Biol.* **193**, 1–12 (2016).
- Russo, C.J. & Passmore, L.A. *Science* **346**, 1377–1380 (2014).
- Zheng, S.Q. *et al. Nat. Methods* **14**, 331–332 (2017).
- Grant, T. & Grigorieff, N. *eLife* **4**, e06980 (2015).
- Rosenthal, P.B. & Henderson, R. *J. Mol. Biol.* **333**, 721–745 (2003).
- Scheres, S.H. *J. Struct. Biol.* **180**, 519–530 (2012).
- Penczek, P.A. *Methods Enzymol.* **482**, 73–100 (2010).
- Davis, J.H. *et al. Cell* **167**, 1610–1622.e15 (2016).
- Penczek, P.A. *J. Struct. Biol.* **138**, 34–46 (2002).
- Sorzano, C.O. *et al. J. Struct. Biol.* **133**, 108–118 (2001).
- Baker, M.R., Fan, G. & Serysheva, I.I. *Eur. J. Transl. Myol.* **25**, 35–48 (2015).

ONLINE METHODS

Protocol for using tilts for single-particle analysis. A general protocol for employing tilts for single-particle data acquisition and analysis is available as a **Supplementary Protocol** and has been deposited into *Protocol Exchange*²². Notably, with the exception of setting the microscope at a defined tilt angle and taking into account the defocus gradient across the micrograph during CTF estimation, all other data collection and image processing operations can be performed normally, as in conventional single-particle analysis.

Statistics. For calculations of Fourier shell correlations (FSC), the FSC cutoff criterion of 0.143 (ref. 15) was used.

Three-dimensional Fourier shell correlation algorithm. We will here describe the meaning of the 3D FSC plot. The usual FSC between two maps (in Fourier space) F and G is given by

$$\text{FSC}(k) = \frac{\sum_{|\vec{k}'|=k} F(\vec{k}')G^*(\vec{k}')}{N_F(k)N_G(k)} \quad (1)$$

Here $|\vec{k}'|$ is the magnitude of the spatial frequency vector \vec{k}' . The normalizations are such that, when F and G agree, then $\text{FSC}(k) = 1$:

$$N_F(k) = \sqrt{\sum_{|\vec{k}'|=k} F(\vec{k}')F^*(\vec{k}')} \quad (2)$$

$$N_G(k) = \sqrt{\sum_{|\vec{k}'|=k} G(\vec{k}')G^*(\vec{k}')} \quad (3)$$

The sums in these expressions are given over all the data k' such that the distance of the points to the Fourier origin is given approximately by k . The meaning of this expression is that FSC is nearly equal to one when the normalized maps are similar. It can be viewed as the cross term of the differences between the normalized maps over the shell. On account of the Friedel symmetry and the integration over the entire shell, the FSC is real.

In the continuous limit, the sum reduces to the integration over a shell of data. If, instead, we wanted to investigate the agreement of F and G over a limited angular range over the shell, then we could alter these quantities to define a conical measure of FSC, which we call 3D FSC. We believe this is essentially the same as the conical measure discussed recently by Diebold *et al.*²³, except a hard cutoff is used here instead of the soft one that introduces another parameter.

$$\text{FSC}_{\delta\theta}(\vec{k}) = \frac{\sum_{|\vec{k}'|=k, |\hat{k}' \cdot \hat{k}| \geq \cos \delta\theta} F(\vec{k}')G^*(\vec{k}')}{N_{F,\delta\theta}(\vec{k})N_{G,\delta\theta}(\vec{k})} \quad (4)$$

$$N_{F,\delta\theta}(\vec{k}) = \sqrt{\sum_{|\vec{k}'|=k, |\hat{k}' \cdot \hat{k}| \geq \cos \delta\theta} F(\vec{k}')F^*(\vec{k}')} \quad (5)$$

$$N_{G,\delta\theta}(\vec{k}) = \sqrt{\sum_{|\vec{k}'|=k, |\hat{k}' \cdot \hat{k}| \geq \cos \delta\theta} G(\vec{k}')G^*(\vec{k}')} \quad (6)$$

Now the sums are performed over all those values of k' that are nearly on the same shell as k and sufficiently close to the direction as governed by the parameter $\delta\theta$. A series of $\delta\theta$ values were tested;

and a value of 20° was chosen, as it provides good averaging properties while still allowing for discrimination of anisotropic FSC patterns. Because of the averaging, the patterns on the surface of a sphere are mostly of a low angular frequency. The result, which is conceptually similar to the conical resolution plots that have been used in tomography^{19,23,24}, is a set of 1D Fourier shell correlation curves computed over distinct angular directions, which can be compiled into a 3D array that we term the 3D FSC. This 3D FSC can be visualized as a 3D density (e.g., in Chimera) and at a fixed threshold value. Here, we chose to present the 3D FSC by showing a central slice through the isosurface (thresholded at 0.143 (ref. 15)), as this helps to show the shape and degree of spherical deformation along the direction of the slice, and the shape and degree in turn represent the degree of directional anisotropy. Alternative representations of directional resolution have also been proposed by Diebold *et al.*²³ and Dudkina *et al.*²⁴. Our numerical implementation is indeed a straightforward modification of the FSC/FRC code in SPARX²⁵/EMAN2 (ref. 26). This 3D FSC evaluation, which is performed in Fourier space and measures directional resolution, is distinct from local resolution measures^{25,27}, which have no relationship to direction. The two metrics are independent of, but complementary to, one another.

In order to quantify the degree of anisotropy of this 3D FSC, spherical Fibonacci mapping using 100 points was performed. The first crossing at a FSC of 0.143 (ref. 15) was used to determine the resolution at these 100 points; and a histogram of these points was plotted, along with the spread of directional resolution values defined by $\pm 1\sigma$ from the mean. Sphericity was also used as a measure of the degree of anisotropy. To calculate sphericity, the 3D FSC was first thresholded (at 0.5) and Gaussian smoothed by 2 pixels in Chimera. Thereafter, the volume and surface area of this smoothed volume was derived and used to calculate the sphericity using the formula²⁸ below:

$$\text{Sphericity} = \frac{\pi^{1/3}(6 \times \text{volume})^{2/3}}{\text{Surface area}} \quad (7)$$

Synthetic data set. A molecular PDB model of the HA trimer (PDB: 3WHE) was first converted to a 2.62 Å density map using EMAN²⁶. 10,000 synthetic particles were then projected from the molecular density map at specific theta angles 30° , 60° , and 90° and with a uniform 5° distribution of phi angles. A fourth data set was generated with uniform distribution of theta and phi projection directions at 5° increments. The synthetic data was generated as previously described²⁹. Briefly, the projections were randomly rotated (randomizing the psi Euler angle) and shifted, followed by the addition of white Gaussian noise, modulation of the noisy images by a contrast transfer and envelope function, and another layer of white Gaussian noise. The final signal-to-noise ratio was estimated at ~ 0.05 , in accordance with real cryo-EM data³⁰.

In order to simulate real experimental errors during reconstruction and mimic the effects of Euler angle uncertainty, all Euler angles and both X and Y shifts were randomly perturbed. The perturbation value was randomly selected from a Gaussian distribution with a mean of 0 and a s.d. of $\pm 4^\circ$ for all Euler angles and ± 2 pixels for all shifts; the true Euler angles and shift values were then modified by adding the above perturbation. Following perturbation, two rounds of FREALIGN^{29,31} refinement were performed.

For masking, a circular mask 160 Å in diameter made using EMAN²⁶ and given a soft Gaussian edge of 6 pixels using apply_mask.exe (distributed with FREALIGN) was applied. FSC between the masked half maps was calculated using EMAN.

Materials, instrumentation, and data acquisition for HA Trimer and LSU_{bl17dep}. The recombinantly expressed and purified H3N2 Hong Kong hemagglutinin trimer (A/Hong Kong/1/1968) was obtained from MyBioSource (catalog number: MBS434205). 3 µl of the sample at 0.75 mg/ml was added to a plasma-cleaned (Gatan Solarus) 1.2 µm hole, 1.3 µm spacing holey gold grid (made in house) and plunge frozen in liquid ethane using the CryoPlunge 3 system (Gatan) operating at >80% humidity, 298 K ambient temperature. The bacterial large ribosomal subunit depleted of bl17 protein (LSU_{bl17dep} sample) was obtained by growing *E. coli* cells without the L17 gene, supplanted with a titratable plasmid containing the L17 gene, with details described in ref. 18. The cells were lysed and the crude lysate separated with a sucrose gradient. 3 µl of the fraction containing the intermediates was concentrated using a 100 kDa MW filter (Amicon) and vitrified in the same manner as the HA trimer.

Both samples were imaged on a Titan Krios electron microscope (FEI) equipped with a K2 summit direct detector (Gatan) at 1.31 Å per pixel in counting mode using the Legion software package³². The HA trimer sample was collected at a dose of ~82 e⁻/Å² across 100 frames for a dose rate of ~7.0 e⁻/pix/sec, using a defocus range of -0.75 µm to -3 µm, with data being acquired over four sessions. A total of 2,469 raw micrographs were collected. The LSU_{bl17dep} sample was collected at a dose of ~34 e⁻/Å² across 50 frames for a dose rate of ~5.8 e⁻/pixel/s using a defocus range of -0.8 µm to -2 µm, with data being acquired over three sessions. A total of 3,906 raw micrographs were collected. Movies were collected from 0° to 50° tilt at 10° increments. The negative tilt side of the goniometer was used, as it is the more stable tilt direction of this particular microscope's goniometer.

Data processing for per-tilt analysis of HA Trimer and LSU_{bl17dep}. For the first set of single-particle analyses at all the various tilts from 0° to 50° (per-tilt analysis, **Supplementary Figs. 4, 7–10**), the first three sessions for the HA trimer sample (consisting of 121 0°, 131 10°, 569 20°, 218 30°, 242 40°, and 237 50° micrographs) and all the three sessions for the LSU_{bl17dep} sample (consisting of 1,220 0°, 574 10°, 559 20°, 449 30°, 527 40°, and 577 50° micrographs) were used.

For both samples, CTF estimation was performed initially with CTFFind3 and CTFTilt³³. Particle extraction was performed reference-free first using DoG picker³⁴. 2D classification was then performed using Xmipp CL2D³⁵. Good class averages were then selected and used for template picking with FindEM³⁶. 2D classification was then performed again with Xmipp CL2D. Initial models for both samples using 2D classification class averages were generated *ab initio* using Optimod³⁷. All these software packages were accessed through the Appion pipeline³⁸.

A total of 364,949 particles for the HA trimer sample and 332,546 particles for the LSU_{bl17dep} sample were obtained after 2D classification. For analysis of the data set, an equal number of particles from micrographs at each tilt angle (0°, 10°, 20°, 30°, 40°, and 50°) were randomly selected, resulting in 155,172 particles for the HA trimer data set and 150,018 particles for the LSU_{bl17dep}

data set (25,862 and 25,003 particles per tilt angle, respectively). For both samples, the selected particles were pooled together and iteratively classified in 3D in order to remove bad particles; for the LSU_{bl17dep} sample, 3D classification additionally produced four distinct superclasses of intermediates (B, C, D, and E¹⁸). Finally, the particles from both data sets were again equalized to ensure the distributions of defocus values were consistent across tilts (0°, 10°, 20°, 30°, 40°, and 50°). This resulted in a total of 78,000 HA trimers (13,000 particles each tilt) and 5,400 particles for each supergroup B, C, D, E, and for each tilt angle within the LSU_{bl17dep} data set.

For both HA and LSU_{bl17dep}, CTFs were estimated using either CTFFind3 alone, CTFFind3 for untilted micrographs and CTFTilt for tilted micrographs (when using CTFFind3 or CTFTilt, the per-particle CTFs were computed using the geometric extrapolation based on the average CTF across the micrograph, nominal tilt angle, and an experimentally derived tilt axis), and GCTF¹¹. In our hands, GCTF provided the best resolution for both HA and LSU_{bl17dep} samples and it was therefore used for all subsequent studies herein. We also evaluated different motion correction programs (Unblur¹⁴, Rubinstein & Brubaker³⁹, and MotionCor2 (ref. 13)), with and without exposure weighting¹⁴, and a standardized refinement (see below) was performed. In our hands, for all five reconstructions, MotionCor2 with exposure weighting produced the highest resolution and was used for subsequent analysis.

In order to refine particles from the individual tilts *ab initio* and separately from one another, the HA trimer reconstruction at this stage was low-pass filtered to 30 Å and used as an initial model for Relion refinement of each individual data set from tilted images. The same was done for the LSU_{bl17dep}, except the model was low-pass filtered to 40 Å. Using these initial models, Relion 3D refinements were performed for each of the five data sets (HA trimer, LSU_{bl17dep} class B, C, D, and E) collected from each individual tilt (0°, 10°, 20°, 30°, 40°, and 50°). The mask for the HA trimer was generated using the HA trimer initial model, which was low-pass filtered, binarized, extended by 9 pixels using 'relion_mask_create', and modified with a soft Gaussian edge of 6 pixels using apply_mask.exe (distributed with the FREALIGN software suite). The mask for all four LSU_{bl17dep} classes was created using the B-class initial model, as it comprises the homogeneous region across all four LSU_{bl17dep} superclasses (details described in ref. 18). The model was binarized and extended by 2 pixels using relion_mask_create and given a soft Gaussian edge of 4 pixels using apply_mask.exe.

The FSC between the masked half maps was calculated using EMAN²⁶. Sharpening of the reconstructions was performed using bfactor.exe, which is distributed with FREALIGN. The best bfactor value was deduced by visual inspection of the map after sharpening with bfactor values in multiples of 50. In order to calculate the map-to-model FSC, the atomic structure of H3N2 HA Trimer (PDB: 3WHE) and the atomic structure of the ribosomal proteins and rRNA helices (PDB: 4YBB) present in all four LSU_{bl17dep} superclasses¹⁸ were used for their respective reconstructions. For the latter, the rationale for only using ribosomal proteins and rRNA helices present in all superclasses is to ensure any observed map differences are not due to structural heterogeneity. The models were converted to density maps at 2.62 Å using Chimera⁴⁰ and aligned to the reconstruction. The density map was then binarized to a mask

using EMAN and then applied to the sharpened reconstruction with a soft Gaussian edge of 6 pixels using `apply_mask.exe`. The FSC between the model density map and the masked reconstructions was calculated using EMAN to give the map-to-model FSC. Similar relative results for all resolution calculations were obtained using shaped masks (as above) and spherical masks, although the exact FSC values differed slightly.

Data processing comparing 0° and 40° tilts for HA trimer analysis. For the second set of single-particle analyses for the HA trimer from micrographs collected at 0° and 40° tilt (**Fig. 1a**), all four sessions for the HA trimer sample (consisting of 466 0° and 847 40° micrographs) were used. Using the 20 most populated 2D Relion class averages, Gautomatch (developed by K. Zhang) was used to select particles, with 226,468 particles picked for 0° micrographs (~486 picks per micrograph) and 287,820 particles picked for 40° micrographs (~340 picks per micrograph). The discrepancy in the average number of selected particles between the 0° and 40° micrographs is caused by the use of the same particle-picking parameters for both sets of data sets for consistency. By visual inspection, more particles could have been picked from the 40° micrographs; but because there were already more particles selected from these than from the 0° micrographs, the particle-picking parameters were not further optimized. Manual masking of bad regions resulted in 214,490 particle picks left for 0° micrographs and 235,049 particle picks left for 40° micrographs. Per-particle CTF was used for CTF estimation, and MotionCor2 with exposure weighting was applied for motion correction. Two rounds of 2D classification were then performed, first using Xmipp CL2D (within the Appion framework) and then using Relion 2D, and bad class averages were discarded, resulting in 137,701 0° tilt particles and 158,432 40° tilt particles. Particles from both data sets were then equalized to ensure the distributions of defocus values were consistent across tilts, resulting in two 130,000 particle stacks for 0° and 40° tilt. Both particle stacks were put through Relion 3D refinement using the standard HA trimer initial model used in the per-tilt analysis. Sharpening, masking, half-map FSC, and map-to-model FSC calculations were performed as described above for the per-tilt analysis.

For the combined data set (**Fig. 1b**), the two equalized stacks of 130,000 particles from micrographs at 0° and 40° tilt were merged to form a stack of 260,000 particles and put through the same refinement and postprocessing procedure as above.

Data processing for *ab initio* 40°-tilt HA trimer. For the *ab initio* 40°-tilt HA-trimer reconstruction (**Fig. 2**), the full stack of 158,432 particles from micrographs at 40° tilt from the HA trimer (0° and 40°) analysis was used. CryoSPARC⁴¹ was used to generate an *ab initio* model. Using a 30 Å low-pass filtered version of this model, the particles were refined using Relion 3D refinement. After the first round of refinement, particles with a maximum probability score of under 0.07 (ref. 42) were removed, resulting in a stack of 125,077 particles. These particles were put through a final round of Relion 3D refinement using a 15 Å low-pass filtered reconstruction from the first round of refinement.

Data processing for *ab initio* 50°-tilt LSU_{BL17dep}. For the *ab initio* 50°-tilt LSU_{BL17dep} reconstruction (**Supplementary Fig. 12**), an *ab initio* initial model was generated from all the particles from micrographs at 50° tilt from per-tilt analysis (17,170 in total) using SIMPLE⁴³. The rationale for combining the particles was to obtain the highest possible resolution for the most homogeneous regions of the data set at a high tilt angle. The initial model was low-pass filtered to 40 Å and used for Relion 3D refinement. The resulting Euler angles from this Relion 3D refinement were then converted to Frealign for ten further rounds of mode 1 refinement and five more rounds of mode 3 refinement with DANG of 3. The masking, sharpening, and FSC calculations were identical to the other LSU_{BL17dep} reconstructions. Local resolution was estimated using the `sxlocres.py` function within the SPARX²⁵ package.

Code availability. The 3D FSC program for calculating directional resolution can be downloaded from <https://github.com/nysbc/Anisotropy> and is available as **Supplementary Software**.

Data availability statement. The 4.2 Å HA trimer map reconstructed using 125,077 best particles from 40°-tilted micrographs is deposited in the EMDB under accession number 8731. The deposition includes the sharpened map, mask, unfiltered half maps, unfiltered map and 3D FSC volume. Raw frames, micrographs, stacks, resulting reconstructions, and associated metadata for the following data sets have also been deposited into the EMPIAR database: 130,000 HA particles from collected at 0° tilt (EMPIAR ID 10096) and 130,000 HA particles collected at 40° tilt (EMPIAR ID 10097).

- Lyumkis, D., Tan, Y.Z. & Baldwin, P.R. *Protoc. Exch.* <http://dx.doi.org/10.1038/protex.2017.055> (2017).
- Diebolder, C.A., Faas, F.G., Koster, A.J. & Koning, R.I. *J. Struct. Biol.* **190**, 215–223 (2015).
- Dudkina, N.V., Kudryashev, M., Stahlberg, H. & Boekema, E.J. *Proc. Natl. Acad. Sci. USA* **108**, 15196–15200 (2011).
- Hohn, M. *et al. J. Struct. Biol.* **157**, 47–55 (2007).
- Tang, G. *et al. J. Struct. Biol.* **157**, 38–46 (2007).
- Kucukelbir, A., Sigworth, F.J. & Tagare, H.D. *Nat. Methods* **11**, 63–65 (2014).
- Wadell, H. *J. Geol.* **43**, 250–280 (1935).
- Lyumkis, D., Brilot, A.F., Theobald, D.L. & Grigorieff, N. *J. Struct. Biol.* **183**, 377–388 (2013).
- Baxter, W.T., Grassucci, R.A., Gao, H. & Frank, J. *J. Struct. Biol.* **166**, 126–132 (2009).
- Grigorieff, N. *J. Struct. Biol.* **157**, 117–125 (2007).
- Suloway, C. *et al. J. Struct. Biol.* **151**, 41–60 (2005).
- Mindell, J.A. & Grigorieff, N. *J. Struct. Biol.* **142**, 334–347 (2003).
- Voss, N.R., Yoshioka, C.K., Radermacher, M., Potter, C.S. & Carragher, B. *J. Struct. Biol.* **166**, 205–213 (2009).
- Sorzano, C.O. *et al. J. Struct. Biol.* **171**, 197–206 (2010).
- Roseman, A.M. *J. Struct. Biol.* **145**, 91–99 (2004).
- Lyumkis, D., Vinterbo, S., Potter, C.S. & Carragher, B. *J. Struct. Biol.* **184**, 417–426 (2013).
- Lander, G.C. *et al. J. Struct. Biol.* **166**, 95–102 (2009).
- Rubinstein, J.L. & Brubaker, M.A. *J. Struct. Biol.* **192**, 188–195 (2015).
- Pettersen, E.F. *et al. J. Comput. Chem.* **25**, 1605–1612 (2004).
- Punjani, A., Rubinstein, J.L., Fleet, D.J. & Brubaker, M.A. *Nat. Methods* **14**, 290–296 (2017).
- Campbell, M.G., Veessler, D., Cheng, A., Potter, C.S. & Carragher, B. *eLife* **4**, e06380 (2015).
- Elmlund, D. & Elmlund, H. *J. Struct. Biol.* **180**, 420–427 (2012).